Boundary-Layer Meteorology (2025) 191:32
https://doi.org/10.1007/s10546-025-00918-9

RESEARCH ARTICLE

A Robust Threshold Method of Mixed Layer Height Based on Lidar Turbulence Data Under Different Thermal Convection Conditions

Lu Wang[1] · Fan He[1] · Jinlong Yuan[2] · Guohua Hu[1] · Jian Mei[1] · Shengliang Han[1] · Lei Hong[1] · Haiyun Xia[2,3]

Received: 13 February 2025 / Accepted: 3 June 2025

Abstract
The mixed layer height (MLH) plays a key role in the atmospheric numerical simulation and environmental assessment. Although the medium threshold (MT) method for retrieving the MLH from lidar turbulence data is promising, the retrieval suffers from the interferences of the low-level jets close to the ground under weak thermal convection conditions and the boundary layer clouds topped on a well-mixed layer under strong thermal convection conditions. Here, a robust threshold (RT) method is developed and demonstrated to be robust against the interferences. It helps recalibrate the MLH by taking account into the influences of the low-level jets and the boundary layer clouds. To evaluate the performance of the RT method, a field experiment is conducted with a coherent Doppler wind lidar. In the experiment, the typical turbulence profiles and their MLH retrieval results under different thermal convection conditions are analyzed. The diurnal variations of the MLH retrieval results by the MT method and the RT method are compared qualitatively and quantitatively. The experiment results indicate that the developed method is more robust to the interferences and thus more suitable for retrieving the MLH under different thermal convection conditions.

Keywords Mixed layer height · Turbulent kinetic energy dissipation rate · Coherent doppler wind lidar · Thermal convection condition

✉ Jinlong Yuan
yuanjinlong@nuist.edu.cn

[1] School of Advanced Manufacturing Engineering, Hefei University, Hefei 230601, China

[2] School of Atmospheric Physics, Nanjing University of Information Science andTechnology, Nanjing 210044, China

[3] School of Earth and Space Science, University of Science and Technology ofChina, Hefei 230026, China

Published online: 25 July 2025

1 Introduction

In the case of fair-weather days, the atmospheric boundary layer (ABL) has a diurnal cycle consisting of the mixed layer (ML) also called the convective boundary layer (CBL) during daytime and a shallow surface ML, the stable boundary layer (SBL), and the above residual layer (RL) during nighttime (Stull 1988; Collaud Coen et al. 2014; Dang et al. 2019; Wang et al. 2021). The ML is one of the major components of the ABL in which we live and breathe at night. In the mixed layer, the main form of motion is turbulence which is usually thermal convectively driven. Thermal convective sources include heat transfer from a warm ground surface after sunrise (Stull 1988). Due to the presence of thermal convection turbulence, mass, and energy, such as heat, water vapor, aerosols, and pollutants are vertically mixed below the mixed layer top (Luo et al. 2014). The mixed layer height (MLH), defined as the height of the mixed layer top, determines the air volume available for the vertical mixing (Seibert et al. 2000). The MLH is thus an essential variable in numerical simulation and environmental assessment of the atmosphere (Yang et al. 2017; Su et al. 2020).

Numerous instruments have been applied to measure the MLH. Direct measuring instruments include radiosondes, meteorological towers, tethered balloons, and aircrafts. Remote measuring instruments include microwave radiometers, sodars, radars, lidars, and satellites. The advantages and shortcomings of the ABL height including the MLH measuring instruments are summarized in Dang et al. (2019), Zhang et al. (2020) while (Seibert et al. 2000) only summarize the MLH measuring instruments. Then, the measurement variables can be used as tracers such as meteorological variables, aerosol-related variables, and turbulence-related variables. Based on these tracers, various retrieval methods have been developed, including the visual method, the idealized profile method, the threshold method, the gradient method, the wavelet method, and the variance method. The ABL height retrieval methods are evaluated in Luo et al. (2014), Collaud Coen et al. (2014), Dang et al. (2019), Kotthaus et al. (2023) while Emeis et al. (2008), Li et al. (2017) only evaluate the MLH retrieval methods.

Specifically, among these MLH retrieval methods, the visual method has subjective errors, while the latter five methods are more common. The idealized profile method is less sensitive to local profiles but not suitable for all atmospheric conditions (Steyn et al. 1999; Eresmaa et al. 2006). The threshold method is simple, though it suffers from the need to define an appropriate threshold value (Dupont et al. 1994). The gradient method is objective but interfered by noises and multiple layers (Sicard et al. 2006). The wavelet method is automated but still interfered by multiple layers (Cohn and Angevine 2000). The variance method is less sensitive to noises, though the temporal resolution of the MLH retrieval results is lower (Piironen and Eloranta 1995).

To improve the atmospheric numerical simulation and environmental assessment, accurate instantaneous MLH from robust techniques is required. Thanks to the recent advances in measuring instruments and retrieval methods, diurnal observations of the MLH are increasingly possible (Zhang et al. 2020; Kotthaus et al. 2023). In terms of measuring instruments, the high spatiotemporal resolution makes lidar one of the most suitable instruments for analyzing the atmosphere boundary layer structure (Chan 2011; Jiang et al. 2022, 2023; Xia et al. 2024; Su et al. 2024). Above the mixed layer, an important feature is the entrainment zone, a zone that is not fully mixed and where turbulence intensity decreases towards its top (Seibert et al. 2000). Thus, in terms of retrieval methods, the threshold method is suit-

able when the tracer is turbulence intensity. The MLH can be retrieved from lidar-measured turbulence intensity vertical profiles by setting an appropriate turbulence intensity threshold (O'Connor et al. 2010; Vakkari et al. 2015; Borque et al. 2016; Manninen et al. 2018; Banakh et al. 2021).

Turbulence intensity is generally characterized by wind velocity variance or turbulent kinetic energy dissipation rate (TKEDR) (Stull 1988; Banakh et al. 2021). For wind velocity variance, the threshold value for retrieving the MLH is found to vary with different locations (Tucker et al. 2009; Pearson et al. 2010; Huang et al. 2017; Wang et al. 2019). For TKEDR, previous studies suggest 10^{-4} m^2 s^{-3} as a suitable threshold value for retrieving the MLH (O'Connor et al. 2010; Vakkari et al. 2015; Borque et al. 2016; Manninen et al. 2018; Banakh et al. 2021). In our previous studies, we demonstrate that TKEDR is a good tracer (Wang et al. 2021) and the suitable threshold value is constant at both inland and marine sites (Wang et al. 2022). Specifically, compared to the tracer of carrier-to-noise ratio (CNR), the tracer of TKEDR is demonstrated that is robust to the lidar instability in MLH retrieval processes (Wang et al. 2021). The effectiveness of the TKEDR threshold value of 10^{-4} m^2 s^{-3} is verified by comparison with radiosondes (Wang et al. 2022).

Although the threshold method for retrieving the MLH from lidar-measured TKEDR vertical profiles is promising, the retrieval suffers from profile fluctuations. A medium threshold (MT) method is applied in Wang et al. (2021) to reduce the influence of profile fluctuations. Nevertheless, the MLH retrieval results by the MT method are sometimes overestimated under weak thermal convection conditions and cannot be detected under strong thermal convection conditions. To solve the issue, a robust threshold (RT) method is developed here.

In this work, to evaluate the performance of the developed method, a field experiment is conducted with a coherent Doppler wind lidar. An observation of TKEDR is then performed. Based on this, the MT method and the RT method are both applied to retrieve MLH from the lidar-measured TKEDR vertical profile. After that, the two MLH retrieval results are compared qualitatively and quantitatively.

The rest of this paper is organized as follows: Sect. 2 introduces the experimental site, instrument, and data. Section 3 describes the MT method and the RT method. Section 4 presents the diurnal variations of the MLH retrieval results by the MT method and the RT method. A statistical comparison of the two MLH retrieval results is also made. Section 5 gives a conclusion. In this paper, LST (local standard time, LST = UTC + 8) is used.

2 Site, Instrument, and Data

2.1 Experimental Site

Figure 1 shows the elevation map of the ground-based experimental site and the figure of the experimental setup. The experiment is conducted at Xilinhot, Xilinguole grassland, China (43°54′N, 115°58′E). It is a remote suburban grassland area without any buildings. The territory is flat with an average altitude of 988.5 m and a typical temperate continental climate. The grassland terrain is favorable for the formation of the low-level jet close to the ground. The lidar operates for 14 days during 1–30 September 2019.

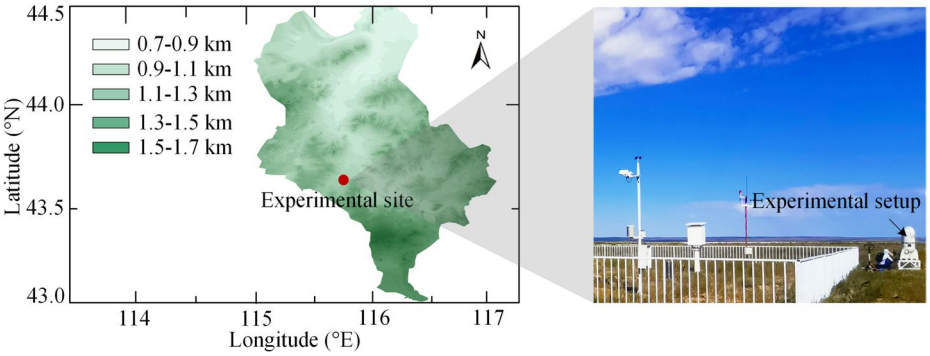

Fig. 1 Elevation map of the experimental site and the figure of the experimental setup

2.2 Coherent Doppler Wind Lidar

In the experiment, a lidar is located on the experimental site. It is an all-fiber coherent Doppler wind lidar. The detailed specifications of the lidar are described in Wang et al. (2017). This lidar is equipped with a rotatable platform and thus has the capability of full hemispheric scanning. During the experiment, the lidar operates in a velocity azimuth display (VAD) mode. This mode is defined as a conical scanning of the laser beam around the vertical axis, with a fixed zenith angle and an azimuth angle that changes from 0 to 360°. In this experiment, the elevation angle is set to 60° and the azimuth angle resolution is set to 5°. The accumulation time of each radial is 2 s thus the cycle time of one conical scan is about 144 s. The radial range resolution is 30 m between 0 and 2.5 km and 60 m between 2.5 and 5.5 km.

2.3 Lidar Data

The main lidar data for retrieving the MLH is TKEDR. After one conical scan of the lidar, a TKEDR vertical profile is obtained. Specifically, for each radial velocity measurement, the aerosol backscatter is first mixed with a local oscillator, resulting in a Doppler signal from which radial wind velocity can be measured. The ratio of Doppler signal power to noise power is CNR which determines the accuracy of radial velocity measurement. Since velocity variance mainly depends on CNR, only the radial velocity measurements with CNR larger than −35 dB (velocity variance smaller than 0.2 m/s) are used for wind vector determination (Wang et al. 2017). Secondly, for one conical scan, the wind vector, including horizontal wind speed, horizontal wind direction, and vertical wind speed, is determined by the filtered sine wave fitting method (Banakh et al. 2010). The percentage of good radial velocity measurements among all measurements over one conical scan is the maximum of the filtering function (Q). To ensure the reliability of wind vectors, the condition of Q_{max} larger than 40% need be satisfied (Banakh et al. 2015). Thirdly, TKEDR, which represents the rate of energy cascades from large to small eddies within the inertial subrange (Borque et al. 2016), is determined by fitting the azimuth structure function of radial wind velocity to a model prediction. The detailed algorithm is described in Smalikho and Banakh (2017).

3 Methodology

3.1 MT Method for Retrieving the MLH

Figure 2 gives two typical TKEDR profiles and their MLH retrieval results under two moderate thermal convection conditions, while Fig. 3 presents two profiles under weak and strong thermal convection conditions respectively. For each row, from left to right are profiles of CNR, Haar wavelet covariance transform of the CNR, horizontal wind speed, TKEDR and its MLH retrieval result by the MT method, and the same TKEDR and its MLH retrieval result by the RT method. MLH_{MT} and MLH_{RT} denoted by black circles and pink circles are the MLH retrieval results by the MT method and the RT method, respectively.

The CNR, which represents aerosol concentration, is a measure of aerosol backscatter intensity. There is usually a rapid increase in a CNR profile at the cloud base, resulting in a local minimum in its Haar wavelet covariance transform profile (Baars et al. 2008). Thus, the Haar wavelet covariance transform (W_f) of CNR is calculated here to identify the cloud base. The Haar function is defined as:

$$h\left(\frac{z-b}{a}\right) = \begin{cases} +1, & b-a/2 \le z \le b \\ -1, & b \le z \le b+a/2 \\ 0, & elsewhere \end{cases} \tag{1}$$

where z is height, a is function dilation, and b is center position. The covariance transform of the function is defined as Brooks (2003):

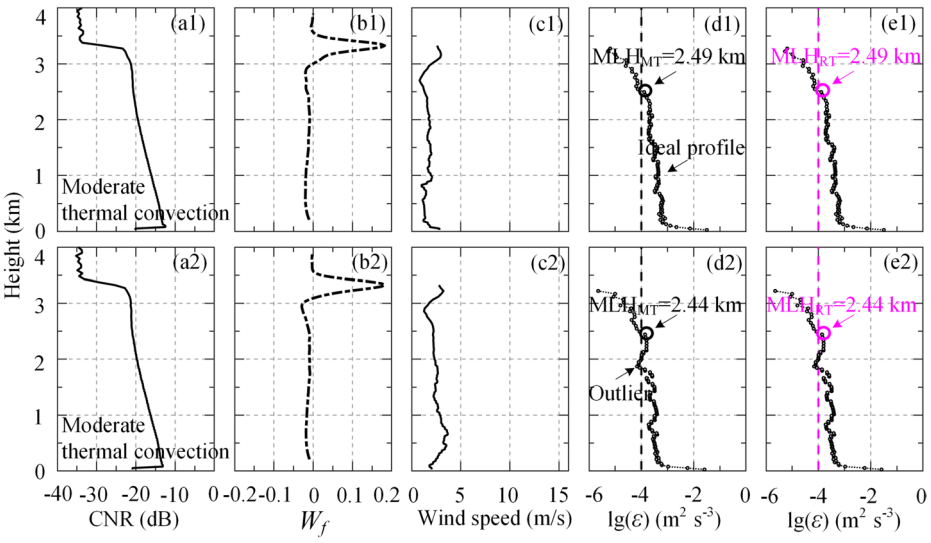

Fig. 2 Profiles of lidar data and their MLH retrieval results on 2 September 2019: **a1** CNR and its **b1** Haar wavelet covariance transform, **c1** horizontal wind speed, **d1** TKEDR base 10 logarithm and MLH_{MT} by the MT method (black circle), **e1** the same TKEDR base 10 logarithm and MLH_{RT} by the RT method (pink circle) under one moderate thermal convection condition. **a2**–**e2** is under the other moderate thermal convection condition

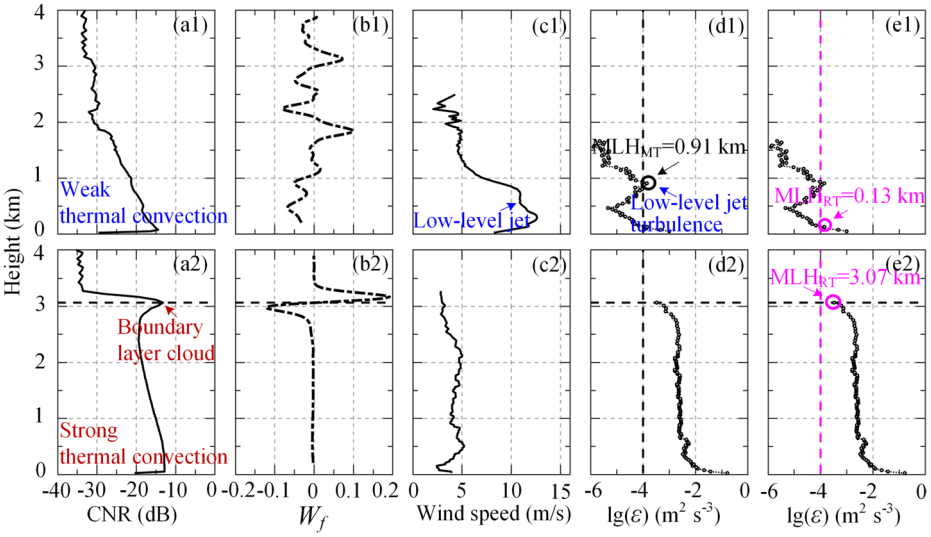

Fig. 3 Profiles of lidar data and their MLH retrieval results on 2 September 2019: **a1** CNR and its **b1** Haar wavelet covariance transform, **c1** horizontal wind speed, **d1** TKEDR base 10 logarithm and MLH_{MT} by the MT method (black circle), **e1** the same TKEDR base 10 logarithm and MLH_{RT} by the RT method (pink circle) under a weak thermal convection condition. **a2**–**e2** is under a strong thermal convection condition

$$W_f(a,b) = \frac{1}{a}\int_{z_b}^{z_t} f(z)\, h\left(\frac{z-b}{a}\right) dz, \tag{2}$$

where $f(z)$ is range-corrected CNR, z_b and z_t are bottom and top heights of selected range.

In theory, for an appropriate threshold, the TKEDR is less than the threshold above the MLH and vice versa. Figure 2d1 gives an ideal TKEDR profile, which is relatively smooth, in moderate thermal convection. The suggested TKEDR threshold of 10^{-4} m^2 s^{-3} in O'Connor et al. (2010, Vakkari et al. (2015), Borque et al. (2016), Manninen et al. (2018), Banakh et al. (2021) is used and hence an MLH of 2.49 km is obtained.

In practice, the retrieval suffers from the interference of profile fluctuations when TKEDR profiles are non-ideal. For example, as seen in Fig. 2d2, there is an outlier caused by profile fluctuations. If the threshold is directly used, the MLH would be mistakenly located at the height of the outlier. An MT method is applied (Wang et al. 2021) to exclude the outlier. In detail, step1, find the median z_{med} of all heights with TKEDR less than the threshold. Step2, find the MLH, which is the maximum of all heights below z_{med} with TKEDR more than the threshold. As a result, the outlier is excluded, and the MLH_{MT} is successfully located at 2.44 km.

Besides, the retrieval suffers from the other interferences of low-level jets and boundary layer clouds. The two interferences usually occur under weak and strong thermal convection conditions, respectively.

At midnight, thermal convection is weak, and low-level jets are often observed. At this time, thermal convection turbulence is weak. Low-level jet turbulence is rare inside jet streams, while it is usually found near jet streams (Brooks 2003). As an example of weak

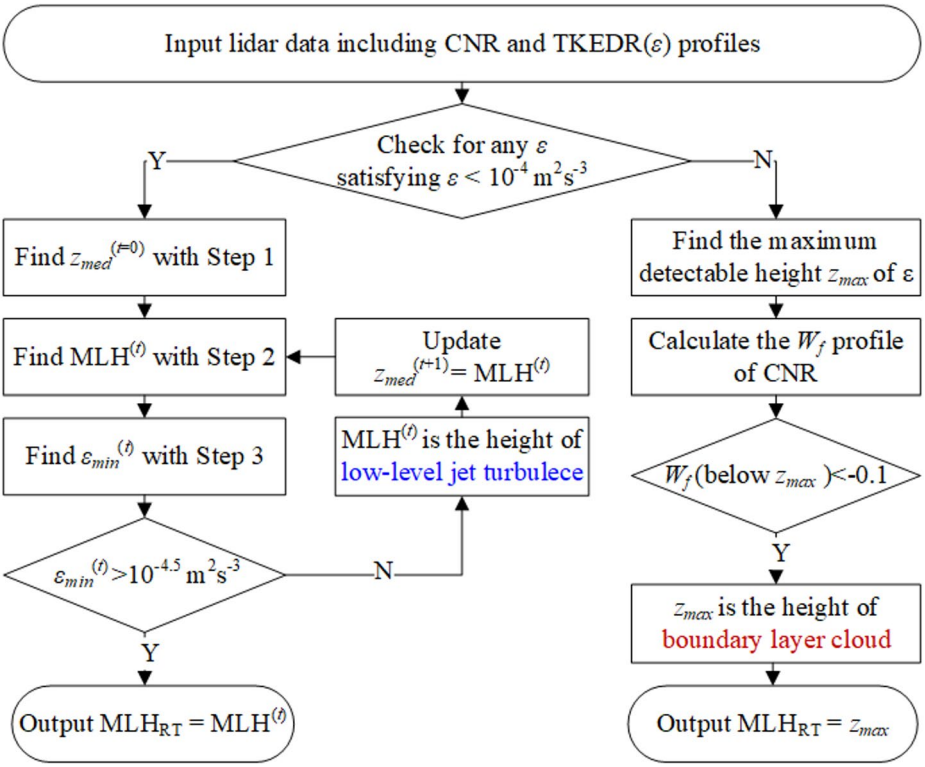

Fig. 4 Workflow of the RT method

thermal convection, Fig. 3d1 gives a TKEDR profile interfered by low-level jet turbulence. As seen in Fig. 3c1, a low-level jet with a maximum wind speed of 12.6 m/s occurs between about 0–0.9 km. The minimum TKEDR at the layer of the maximum wind speed is about $10^{-5.5}$ m^2 s^{-3}. The low-level jet turbulence is then formed above the jet stream, leading to an accidental increase in the TKEDR profile from about $10^{-5.5}$ to $10^{-4.5}$ m^2 s^{-3} between about 0.5–0.9 km. One can see that the MLH_{MT} is overestimated at 0.91 km which is the height of the low-level jet turbulence. It indicates that the MT method is inapplicable when there is a low-level jet close to the ground under weak thermal convection conditions.

At noon, boundary layer clouds are often observed under strong thermal convection conditions. Thermal convection turbulence is dominant because thermal bubbles are the basic form of turbulence (Zhang et al. 2020). On the top of a well-mixed layer, boundary layer clouds are usually formed. As an example of strong thermal convection, Fig. 3d2 gives a TKEDR profile interfered by a boundary layer cloud. As seen in Fig. 3a2, there is a rapid increase in the CNR profile at about 3 km, resulting in a local minimum of less than −0.1 in its Haar wavelet covariance transform profile as seen in Fig. 3b2. The height of the cloud base is identified by the local minimum. The error of TKEDR estimation increases rapidly above the cloud, resulting in the lack of TKEDR estimation above about 3 km as seen in Fig. 3d2. Due to the lack of TKEDR estimation, the MLH_{MT} cannot be detected. It indicates that the MT method is inapplicable when there is a boundary layer cloud topped on a well-mixed layer under strong thermal convection conditions.

In summary, Fig. 2d1 and d2 indicate that the MT method is applicable for retrieving the MLH under moderate thermal convection conditions but Fig. 3d1 and d2 indicate that the MT method is inapplicable under weak and strong thermal convection conditions.

3.2 RT Method for Retrieving the MLH

To resist the interferences of low-level jets and boundary layer clouds, an RT method is developed here. The MLH retrieval process of the RT method takes account into the interferences of the low-level jets under weak thermal convection conditions and the boundary layer clouds under strong thermal convection conditions, which helps recalibrate the retrieval result. The workflow of the RT method is shown in Fig. 4.

Firstly, the lidar data including CNR and TKEDR (ϵ) profiles are input.

Secondly, the suggested ϵ threshold of 10^{-4} m^2 s^{-3} in O'Connor et al. (2010), Vakkari et al. (2015), Borque et al. (2016), Manninen et al. (2018), Banakh et al. (2021) is used. If there is ϵ less than the threshold, the workflow is as follows:

Step 1. Find the median ${z_{med}}^{(t=0)}$ of all heights with ϵ less than the threshold.

Step 2. Find $\mathrm{MLH}^{(t)}$, which is the maximum of all heights below ${z_{med}}^{(t)}$ with ϵ more than the threshold.

Step 3. Find the minimum ${\epsilon_{min}}^{(t)}$ of all ϵ below $\mathrm{MLH}^{(t)}$. Set $\mathrm{MLH_{RT}}$ equal to $\mathrm{MLH}^{(t)}$ if ${\epsilon_{min}}^{(t)} > 10^{-4.5}$ m^2 s^{-3} is satisfied. Otherwise, update ${z_{med}}^{(t+1)}$ as $\mathrm{MLH}^{(t)}$, and then repeat Steps 2 and 3. Considering the minimum TKEDR at the layer of the maximum wind speed in the low-level jet is between about $10^{-4.5}$ and $10^{-5.5}$ m^2 s^{-3} during this observation and having tested multiple limit values, a lower limit of $10^{-4.5}$ m^2 s^{-3} is used here. The lower

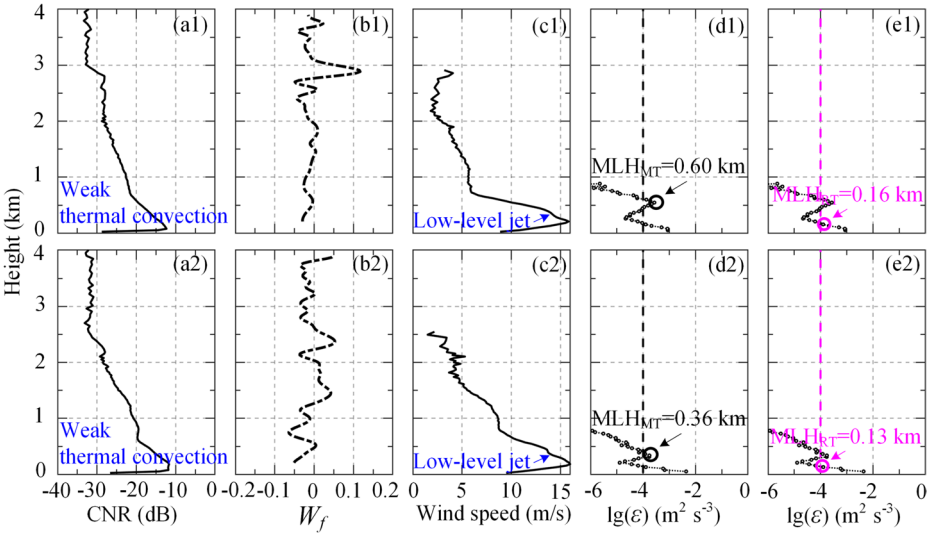

Fig. 5 Profiles of lidar data and their MLH retrieval results: **a1** CNR and its **b1** Haar wavelet covariance transform, **c1** horizontal wind speed, **d1** TKEDR base 10 logarithm and $\mathrm{MLH_{MT}}$ by the MT method (black circle), **e1** the same TKEDR base 10 logarithm and $\mathrm{MLH_{RT}}$ by the RT method (pink circle) under a weak thermal convection condition on 27 September 2019. **a2**–**e2** is under another weak thermal convection condition on 28 September 2019

limit is used to identify whether the $\mathrm{MLH}^{(t)}$ is overestimated at the height of low-level jet turbulence. As a result, in Fig. 3e1, the $\mathrm{MLH_{RT}}$ is successfully located at 0.13 km.

Thirdly, if there is no ϵ less than the threshold, the workflow is as follows:

Find the maximum detectable height z_{max} of ε.

Calculate the Haar wavelet covariance transform (W_f) of CNR (Brooks 2003). The W_f calculated here is to identify boundary layer clouds.

In the case of boundary layer clouds, the cloud height is the boundary layer height (Li et al. 2017). Set $\mathrm{MLH_{RT}}$ equal to z_{max} if $W_f < -0.1$ is satisfied just below z_{max}. An upper limit of −0.1 (Baars et al. 2008) is used to identify cloud bases. In other words, the upper limit is used to identify whether there is a boundary layer cloud at z_{max}. As a result, in Fig. 3e2, the $\mathrm{MLH_{RT}}$ is successfully obtained at 3.07 km.

Finally, the $\mathrm{MLH_{RT}}$ is output.

The reason for the $\mathrm{MLH_{RT}}$ difference between Fig. 3e1 and e2 is that Fig. 3e1 corresponds to a shallow surface ML at midnight whereas Fig. 3e2 corresponds to a fully developed ML at noon. Figures 2e1, e2 and 3e1, e2 indicate that the RT method is suitable for retrieving the MLH under different thermal convection conditions including weak and strong thermal convection conditions. To further evaluate the RT method, Fig. 5 gives the other two low-level jet cases under weak thermal convection conditions. As seen in Fig. 5c1, c2, the low-level jets with a maximum wind speed of 16.0 m/s are both observed. In Fig. 5d1, d2, the $\mathrm{MLH_{MT}}$ are overestimated at 0.60 km and 0.36 km which are the heights of the low-level jet turbulences, whereas the $\mathrm{MLH_{RT}}$ are successfully located at 0.16 km and 0.13 km in Fig. 5e1, e2.

4 Experimental Results and Discuss

4.1 Diurnal Variations of the MLH Retrieval Results by the MT Method and the RT Method

Figure 6 presents a two-day continuous observation of TKEDR and its MLH retrieval results. The short data missing results from the suspension of lidar for cleaning the telescope. From top to bottom are diurnal variations of CNR as shown in Fig. 6a, horizontal wind speed in Fig. 6b, horizontal wind direction in Fig. 6c, vertical wind speed in Fig. 6d, TKEDR and its MLH retrieval result by the MT method in Fig. 6e1, and the same TKEDR and its MLH retrieval result by the RT method in Fig. 6e2. Wind direction is defined as 0° for northerly horizontal wind and rotates clockwise. Positive vertical wind speed denotes downward wind. The sunrise time is marked by red upward triangles, and the sunset time is by blue downward triangles. The $\mathrm{MLH_{MT}}$ and the $\mathrm{MLH_{RT}}$ are still denoted by black circles and pink circles, respectively (Fig. 5).

As seen in Fig. 6e1, there are two obvious diurnal variations in both TKEDR and its MLH retrieval results. In general, turbulence sources include wind shear production and buoyancy production (Moeng and Sullivan 1994). Wind shear production arises from the shear close to the ground wind or is associated with low-level jets at night (Banta et al. 2006; Manninen et al. 2018). During the daytime, buoyancy production is the dominant turbulence source (Oke 2002). After sunrise, thermal convection turbulence develops gradually forced by solar radiation, and boundary layer clouds are usually formed in the upper portion of the mixed layer.

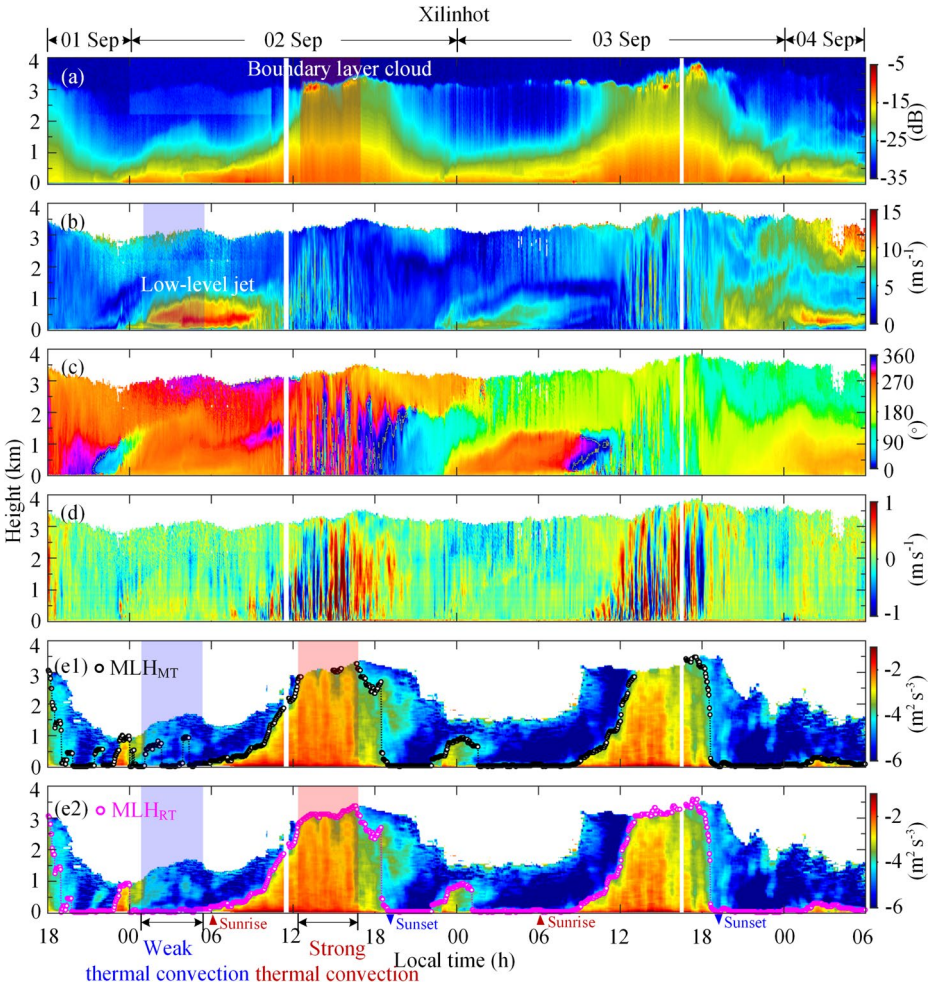

Fig. 6 Diurnal variations of lidar data and their MLH retrieval results during 2–3 September 2019: **a** CNR, **b** Horizontal wind speed, **c** horizontal wind direction, **d** vertical wind speed, **e1** TKEDR base 10 logarithm and MLH_{MT} by the MT method (black circle), **e2** the same TKEDR base 10 logarithm and MLH_{RT} by the RT method (pink circle)

In the nighttime of the two days, low-level jets are both observed during 0000–1000 LST on 2 September and during 0000–0600 LST on 3 September as seen in Fig. 6b. The horizontal wind speed is in the range of 10–15 m/s. The corresponding horizontal wind direction and vertical wind speed are relatively stable as seen in Fig. 6c, d. The first half of the low-level jet on 2 September, which occurs close to the ground and under weak thermal convection conditions, may interfere with the MLH retrieval. Take 2 September as an example, the sunrise time is 0554 LST, while the sunset time is 1902 LST, and the TKEDR reaches its peak at about 1400 LST. As seen in Fig. 6e1, the low-level jet turbulence is formed above the jet stream away from the ground, while the thermal convection turbulence close to the ground is weak before sunrise, resulting in an accidental increase in the TKEDR. It

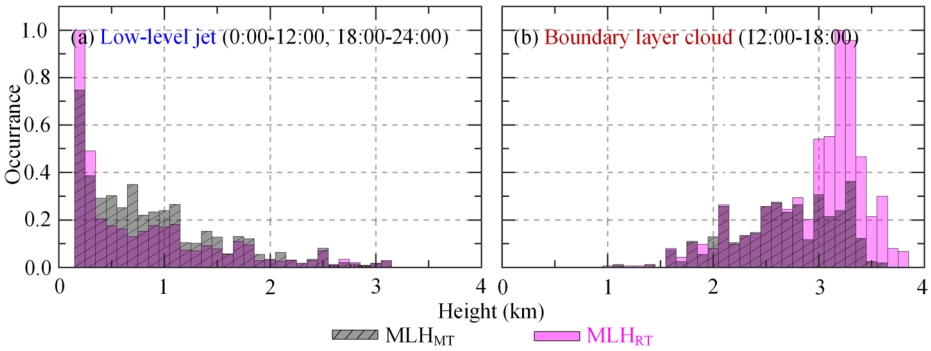

Fig. 7 Statistical comparison of MLH_{MT} (black column) and MLH_{RT} (pink column) in 14 fair weather days during 1–30 September 2019: **a** 0000–1200, 1800–2400 LST including 10 low-level jet cases, **b** 1200–1800 LST including 11 boundary layer cloud cases

is noticeable that the MLH_{MT} in Fig. 6e1 is overestimated at the height of the low-level jet turbulence whereas the MLH_{RT} in Fig. 6e2 is successfully located at the near-surface.

In the daytime of 2 September, boundary layer clouds are observed during 1300–1700 LST at about 3 km as seen in Fig. 6a. The boundary layer cloud, which occurs topped on a well-mixed layer and under strong thermal convections, may interfere with the MLH retrieval. As seen in Fig. 6e1, the TKEDR cannot be detected above the cloud. Note that the MLH_{MT} in Fig. 6e1 cannot be detected due to the lack of TKEDR estimation whereas the MLH_{RT} in Fig. 6e2 is successfully obtained.

4.2 Statistical Comparison of the MLH Retrieval Results by the MT Method and the RT Method

As seen in Fig. 6a and b, the low-level jet is often observed during 0000–1200, 1800–2400 LST, and the boundary layer cloud is during 1200–1800 LST. To further compare the performance of the MT method and the RT method, the MLH_{MT} and the MLH_{RT} are both classified into the two time periods.

Figure 7 shows the statistical distribution of the MLH_{MT} and the MLH_{RT}. The ordinate is the occurrence of MLH retrieval results in the range of 0 and 4 km. The MLH_{MT} and the MLH_{RT} are denoted by black columns and pink columns, respectively. As shown in Fig. 7a, compared to the MLH_{MT}, the occurrence of MLH_{RT} at the near-surface is larger. Correspondingly, the mean of the MLH_{RT} in this time period is 0.39 km which is 0.1 km lower than the MLH_{MT}. It demonstrates the improved reliability of the RT method in correcting the overestimated MLH_{MT} interfered by low-level jets. In Fig. 7b, the occurrence of MLH_{RT} in the range of 3–4 km is larger. The mean of the MLH_{RT} is 2.96 km which is 0.3 km higher than the MLH_{MT}. It demonstrates the improved reliability of the RT method in filling the undetected MLH_{MT} interfered by boundary layer clouds. In a word, Figs. 6b and 7a validate the capability of the RT method in resisting the interferences of low-level jets and boundary layer clouds.

5 Conclusion

A robust threshold method for retrieving the MLH from lidar-measured TKEDR vertical profiles under different thermal convection conditions is developed and demonstrated. To evaluate the anti-interference of the developed method, an observation is performed with a ground-based lidar. The experiment results indicate that the developed method is not only workable under moderate thermal convection conditions but also works well under weak and strong thermal convection conditions. Such a developed method is expected to contribute to improving the accuracy of atmospheric numerical simulation and environmental assessment.

In this work, the performance of the RT method is evaluated in fair weather at single site. To comprehensively evaluate the performance of the RT method, not only fair weather but also other weathers at different sites are needed in further studies.

Acknowledgements The authors are grateful to the anonymous reviewers for their constructive comments.

Author Contributions L.W. performed the post-processing of the data, created the visualizations, interpreted the results, and wrote the original draft. F.H., G.H., J.M., S.H., and L.H. contributed to the conceptualization of the study. J.Y. and H.X. supervised the research, contributed to the discussion and interpretation of results, and reviewed and edited the original draft. All authors have read and agreed to the manuscript.

Funding This work was financially supported by the Natural Science Research Project of Anhui Educational Committee (2023AH052192) and the Talent Research Project of Hefei University (24RC04).

Data Availability Data underlying the results presented in this paper can be obtained from the authors upon reasonable request.

Declarations

Conflict of interest The authors declare no conflict of interest.

References

Baars H, Ansmann A, Engelmann R, Althausen D (2008) Continuous monitoring of the boundary-layer top with lidar. Atmos Chem Phys 8:7281–7296. https://doi.org/10.5194/acp-8-7281-2008

Banakh VA, Brewer A, Pichugina EL, Smalikho IN (2010) Measurements of wind velocity and direction with coherent doppler lidar in conditions of a weak echo signal. Atmos Ocean Opt 23:381–388. https://doi.org/10.1134/S1024856010050076

Banakh VA, Smalikho IN, Falits AV et al (2015) Joint radiosonde and doppler lidar measurements of wind in the atmospheric boundary layer. Atmos Ocean Opt 28:185–191. https://doi.org/10.1134/S1024856015020025

Banakh VA, Smalikho IN, Falits AV (2021) Estimation of the height of the turbulent mixing layer from data of doppler lidar measurements using conical scanning by a probe beam. Atmos Meas Tech 14:1511–1524. https://doi.org/10.5194/amt-14-1511-2021

Banta RM, Pichugina YL, Brewer WA (2006) Turbulent velocity-variance profiles in the stable boundary layer generated by a nocturnal Low-Level jet. J Atmos Sci 63:2700–2719. https://doi.org/10.1175/JAS3776.1

Borque P, Luke E, Kollias P (2016) On the unified Estimation of turbulence eddy dissipation rate using doppler cloud radars and lidars. J Geophys Res Atmos 121:5972–5989. https://doi.org/10.1002/2015JD024543

Brooks IM (2003) Finding boundary layer top: application of a wavelet covariance transform to lidar backscatter profiles. J Atmos Ocean Technol 20:1092–1105

Chan PW (2011) Generation of an eddy dissipation rate map at the Hong Kong international airport based on doppler lidar data. J Atmos Ocean Technol 28:37–49. https://doi.org/10.1175/2010JTECHA1458.1
Cohn SA, Angevine WM (2000) Boundary layer height and entrainment zone thickness measured by lidars and Wind-Profiling radars. J Appl Meteor 39:1233–1247.
Collaud Coen M, Praz C, Haefele A et al (2014) Determination and climatology of the planetary boundary layer height above the Swiss plateau by in situ and remote sensing measurements as well as by the COSMO-2 model. Atmos Chem Phys 14:13205–13221. https://doi.org/10.5194/acp-14-13205-2014
Dang R, Yang Y, Hu X-M et al (2019) A review of techniques for diagnosing the atmospheric boundary layer height (ABLH) using aerosol lidar data. Remote Sens 11:1590. https://doi.org/10.3390/rs11131590
Dupont E, Pelon J, Flamant C (1994) Study of the moist convective boundary layer structure by backscattering lidar | boundary-layer meteorology. Bound Layer Meteorol 69:1–25. https://doi.org/10.1007/BF00713292
Emeis S, Schäfer K, Münkel C (2008) Surface-based remote sensing of the mixing-layer height a review. Metz 17:621–630. https://doi.org/10.1127/0941-2948/2008/0312
Eresmaa N, Karppinen A, Joffre SM et al (2006) Mixing height determination by ceilometer. Atmos Chem Phys 6:1485–1493. https://doi.org/10.5194/acp-6-1485-2006
Huang M, Gao Z, Miao S et al (2017) Estimate of Boundary-Layer Depth Over Beijing, China, Using Doppler Lidar Data During SURF-2015. Bound-Layer Meteorol 162:503–522. https://doi.org/10.1007/s10546-016-0205-2
Jiang P, Yuan J, Wu K et al (2022) Turbulence detection in the atmospheric boundary layer using coherent doppler wind lidar and microwave radiometer. Remote Sens 14:2951. https://doi.org/10.3390/rs14122951
Jiang P, Xia H, Hu J, Wei T (2023) Estimation of atmospheric refractive index structure constant using an ingaas/inp single-photon detector. Opt Lett 48:6104. https://doi.org/10.1364/OL.505631
Kotthaus S, Bravo-Aranda JA, Collaud Coen M et al (2023) Atmospheric boundary layer height from ground-based remote sensing: a review of capabilities and limitations. Atmos Meas Tech 16:433–479. https://doi.org/10.5194/amt-16-433-2023
Li H, Yang Y, Hu X et al (2017) Evaluation of retrieval methods of daytime convective boundary layer height based on lidar data. J Geophys Res Atmos 122:4578–4593. https://doi.org/10.1002/2016JD025620
Luo T, Yuan R, Wang Z (2014) Lidar-based remote sensing of atmospheric boundary layer height over land and ocean. Atmos Meas Tech 7:173–182. https://doi.org/10.5194/amt-7-173-2014
Manninen AJ, Marke T, Tuononen M, O'Connor EJ (2018) Atmospheric boundary layer classification with doppler lidar. J Geophys Res Atmos 123:8172–8189. https://doi.org/10.1029/2017JD028169
Moeng C-H, Sullivan PP (1994) A comparison of shear- and buoyancy-driven planetary boundary layer flows. J Atmos Sci 51:999–1022
O'Connor EJ, Illingworth AJ, Brooks IM et al (2010) A method for estimating the turbulent kinetic energy dissipation rate from a vertically pointing doppler lidar, and independent evaluation from Balloon-Borne in situ measurements. J Atmos Ocean Technol 27:1652–1664. https://doi.org/10.1175/2010JTECHA1455.1
Oke TR (2002) Boundary layer climates. Boundary layer climates. Routledge, LON, UK, pp 3–5
Pearson G, Davies F, Collier C (2010) Remote sensing of the tropical rain forest boundary layer using pulsed doppler lidar. Atmos Chem Phys 10:5891–5901. https://doi.org/10.5194/acp-10-5891-2010
Piironen AK, Eloranta EW (1995) Convective boundary layer mean depths and cloud geometrical properties obtained from volume imaging lidar data. J Geophys Res Atmos 100:25569–25576. https://doi.org/10.1029/94JD02604
Seibert P, Beyrich F, Gryning S-E et al (2000) Review and intercomparison of operational methods for the determination of the mixing height. Atmos Environ 34:1001–1027. https://doi.org/10.1016/S1352-2310(99)00349-0
Sicard M, Pérez C, Rocadenbosch F et al (2006) Mixed-Layer depth determination in the Barcelona coastal area from regular lidar measurements: methods, results and limitations. Bound-Layer Meteorol 119:135–157. https://doi.org/10.1007/s10546-005-9005-9
Smalikho IN, Banakh VA (2017) Measurements of wind turbulence parameters by a conically scanning coherent doppler lidar in the atmospheric boundary layer. Atmos Meas Tech 10:4191–4208. https://doi.org/10.5194/amt-10-4191-2017
Steyn DG, Baldi M, Hoff RM (1999) The detection of mixed layer depth and entrainment zone thickness from lidar backscatter profiles. J Atmos Ocean Technol 16:953–959
Stull RB (1988) An introduction to boundary layer meteorology. An introduction to boundary layer meteorology. Kluwer Academic, Dordrecht, Dordrecht, Netherlands, pp 12–14
Su T, Li Z, Kahn R (2020) A new method to retrieve the diurnal variability of planetary boundary layer height from lidar under different thermodynamic stability conditions. Remote Sens Environ 237:111519. https://doi.org/10.1016/j.rse.2019.111519

Su L, Lu C, Yuan J et al (2024) Measurement report: the promotion of the low-level jet and thermal effects on the development of the deep convective boundary layer at the Southern edge of the Taklimakan desert. Atmos Chem Phys 24:10947–10963. https://doi.org/10.5194/acp-24-10947-2024

Tucker SC, Senff CJ, Weickmann AM et al (2009) Doppler lidar Estimation of mixing height using turbulence, shear, and aerosol profiles. J Atmos Ocean Technol 26:673–688. https://doi.org/10.1175/2008JTECHA1157.1

Vakkari V, O'Connor EJ, Nisantzi A et al (2015) Low-level mixing height detection in coastal locations with a scanning doppler lidar. Atmos Meas Tech 8:1875–1885. https://doi.org/10.5194/amt-8-1875-2015

Wang C, Xia H, Shangguan M et al (2017) 1.5 μm polarization coherent lidar incorporating time-division multiplexing. Opt Express 25:20663–20674. https://doi.org/10.1364/OE.25.020663

Wang C, Jia M, Xia H et al (2019) Relationship analysis of $PM_{2.5}$ and boundary layer height using an aerosol and turbulence detection lidar. Atmos Meas Tech 12:3303–3315. https://doi.org/10.5194/amt-12-3303-2019

Wang L, Qiang W, Xia H et al (2021) Robust solution for boundary layer height detections with coherent doppler wind lidar. Adv Atmos Sci 38:1920–1928. https://doi.org/10.1007/s00376-021-1068-0

Wang L, Yuan J, Xia H et al (2022) Marine mixed layer height detection using Ship-Borne coherent doppler wind lidar based on constant turbulence threshold. Remote Sens 14:745. https://doi.org/10.3390/rs14030745

Xia H, Chen Y, Yuan J et al (2024) Windshear detection in rain using a 30 Km radius coherent doppler wind lidar at mega airport in plateau. Remote Sen 16:924. https://doi.org/10.3390/rs16050924

Yang T, Wang Z, Zhang W et al (2017) Technical note: boundary layer height determination from lidar for improving air pollution episode modeling: development of new algorithm and evaluation. Atmos Chem Phys 17:6215–6225. https://doi.org/10.5194/acp-17-6215-2017

Zhang H, Zhang X, Li Q et al (2020) Research progress on Estimation of the atmospheric boundary layer height. J Meteorol Res 34:482–498. https://doi.org/10.1007/s13351-020-9910-3